Research Article

Insights into Electrochemical CO_2 Reduction on Metallic and Oxidized Tin Using Grand-Canonical DFT and In Situ ATR-SEIRA Spectroscopy

Todd N. Whittaker, Yuval Fishler, Jacob M. Clary, Paige Brimley, Adam Holewinski, Charles B. Musgrave, Carrie A. Farberow, Wilson A. Smith,* and Derek Vigil-Fowler*

Read Online

ACCESS | Metrics & More | Article Recommendations | SI Supporting Information

ABSTRACT: Electrochemical CO_2 reduction (CO_2R) to formate is an attractive carbon emissions mitigation strategy due to the existing market and attractive price for formic acid. Tin is an effective electrocatalyst for CO_2R to formate, but the underlying reaction mechanism and whether the active phase of tin is metallic or oxidized during reduction is openly debated. In this report, we used grand-canonical density functional theory and attenuated total reflection surface-enhanced infrared absorption spectroscopy to identify differences in the vibrational signatures of surface species during CO_2R on fully metallic and oxidized tin surfaces. Our results show that CO_2R is feasible on both metallic and oxidized tin. We propose that the key difference between each surface termination is that CO_2R catalyzed by metallic tin surfaces is limited by the electrochemical activation of CO_2, whereas CO_2R catalyzed by oxidized tin surfaces is limited by the slow reductive desorption of formate. While the exact degree of oxidation of tin surfaces during CO_2R is unlikely to be either fully metallic or fully oxidized, this study highlights the limiting behavior of these two surfaces and lays out the key features of each that our results predict will promote rapid CO_2R catalysis. Additionally, we highlight the power of integrating high-fidelity quantum mechanical modeling and spectroscopic measurements to elucidate intricate electrocatalytic reaction pathways.

CO_2 reduction to formate over Sn catalysts

Metallic Sn — CO_2 activation limited / Facile desorption

Oxidized Sn — Facile CO_2 activation / Desorption limited

KEYWORDS: CO_2 reduction, formic acid production, grand-canonical DFT, ATR-SEIRAS, mechanism evaluation
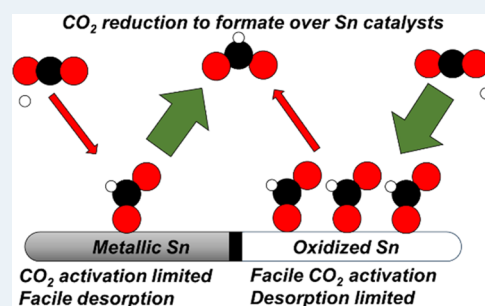
INTRODUCTION

Electrochemical CO_2 reduction (CO_2R) is a potential strategy to lessen the impact of anthropogenic climate change and has been studied extensively across a variety of electrode materials over the last few decades.[1] Copper has received the most attention in the CO_2R literature due to its seemingly unique ability to produce C_{2+} products such as ethylene and ethanol with appreciable Faradaic efficiency, while gold and silver have also been studied for their high selectivity to CO.[2−4] However, a recent technoeconomic analysis showed that under 2019 market conditions, formic acid was the CO_2R product with a production cost closest to break-even.[5] Formic acid, which has an annual global demand of ~800 kilotons and is used mostly as a food preservative and in the production of rubber and leather, is produced at scale via the hydrolysis of formamide, which has undesirable environmental impacts.[6] Therefore, CO_2R to produce formic acid is not only a promising climate solution but can potentially reduce dependence on a nonideal existing industrial process.

CO_2R catalysts that are selective toward formate are generally characterized by having a weak affinity for CO. Most are p-block metals, and, among these, tin (Sn) is the most attractive because it has higher electrochemical stability

than zinc and indium, is more environmentally benign than cadmium or lead, and is more abundant than bismuth.[7,8] There have been many reports of using Sn-based electrocatalysts for CO_2R, generally showing that at potentials more negative than -0.6 V_{RHE}, Faradaic efficiencies of >70% toward formic acid can be achieved with state-of-the-art current densities reaching 500 mA/cm^2.[9−12] However, several reports have shown differing interpretations of the precise nature of the active phase of Sn during CO_2R. Based on the Pourbaix diagram for Sn, the purely metallic phase is expected to be present at potentials more negative than -0.5 V_{RHE}. However, numerous reports have invoked oxide phases of Sn as the active phase,[10,13−20] with some going as far as to say that CO_2R does not proceed on metallic Sn at all.[21−23] In direct opposition to this conclusion, many other reports claim that the metallic phase is the active phase and that in situ reduction
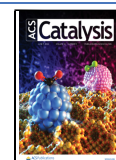
of the oxide material to a more active metallic Sn phase is responsible for the high observed CO_2R activity and selectivity.[9,24,25] Clearly, neither the true surface state nor the mechanism of CO_2R on Sn-based electrocatalysts has been firmly established, and this lack of clarity has limited the development of improved catalysts and reactor systems.

In this report, we use a combined computational chemistry and in situ spectroscopic approach to examine CO_2R on both metallic and oxidized Sn electrodes. While a number of metastable Sn phases exist between the fully metallic Sn^0 and fully oxidized SnO_2 phases that could be responsible for CO_2R activity,[13,21] we chose these end points as useful limiting cases to examine. We use grand-canonical density functional theory (GC-DFT) to investigate the CO_2R mechanism under conditions relevant to the in situ experimental measurements. This approach poses several advantages compared to simpler methods such as the computational hydrogen electrode (CHE) method developed by Nørskov and co-workers almost 20 years ago. While the CHE is elegantly simple and has led to valuable insights into electrocatalytic mechanisms,[26] it also suffers from key limitations, namely that all molecular geometries, including the catalyst adsorbate structures, are relaxed at the potential of zero charge (PZC), that all electron transfers must be charge neutral (e.g., proton-coupled electron transfer, PCET, rather than sequential proton/electron transfer), and that it neglects the potential dependence on energetics of chemical steps.[27−30] GC-DFT accurately describes electrochemical mechanisms due to its self-consistent treatment of the electrified interface under an applied potential and its ability to capture decoupled charge transfer, widely believed to be a relevant elementary step in CO_2R ($CO_2 + * + e^- \rightarrow CO_2^-*$, where * represents a surface active site).[4,30,31] We also use attenuated total reflection surface-enhanced infrared absorption spectroscopy (ATR-SEIRAS) to investigate metallic and oxidized Sn surfaces during electrocatalysis. We recently developed a method of preparing Sn-based films that exhibit excellent surface enhancement in ATR-SEIRAS.[32] Much of the ongoing debate in the community regarding CO_2R on Sn originates from the lack of reliability in preparing and characterizing model Sn surfaces for spectroscopic investigation, as well as ambiguous frequency assignment.[10,21] By carefully comparing our observations from the GC-DFT and ATR-SEIRAS studies, we show that CO_2R is feasible on both metallic and oxidized Sn through a combination of pathways that lead to adsorbed formate. Based on these results, metallic Sn is expected to show stronger competition from the hydrogen evolution reaction (HER) because of its lower affinity for CO_2R intermediates, whereas oxidized Sn is hindered by overbound formate and competition with molecularly adsorbed water and electrolyte ions.

■ METHODS

Materials. All solutions were prepared in 18.2 MΩ deionized water (Elga PURELAB flex 1). CO_2 (4.0, Airgas), Ar (5.0, Airgas), 96% sulfuric acid (Suprapur, Merck), 65% nitric acid (Suprapur, Merck), tin(II) sulfate (≥95%, Sigma-Aldrich), and potassium bicarbonate (Certified ACS Crystalline, Fisher Chemical) were used as received.

ATR-SEIRAS. In situ ATR-SEIRAS experiments were performed on a Nicolet 6700 FTIR spectrometer (Thermo Fisher Scientific) with a VeeMAX III ATR chamber (PIKE Technologies). The spectro-electrochemical experiments were performed in a J1W Jackfish spectro-electrochemical cell

(PIKE Technologies) with a PTFE/PEEK base. The synthesis and characterization of ATR-SEIRAS-active Sn-based films have been described in detail elsewhere.[32] Other reports have also detailed the synthesis of electrodeposited metal films for SEIRAS, but not films of metal oxides.[33,34] Briefly, a polycrystalline Au underlayer was chemically deposited onto a Si(100) specialized 1 ATR element (single-bounce ATR crystal, IRUBIS) according to the procedure reported by Osawa.[35] This underlayer was electrochemically cycled between 0.2 and 1.75 V_{RHE} at 50 mV/s for 20 cycles with a Au counter electrode to achieve a clean, SEIRAS-active film. Metallic Sn was electrodeposited onto the Au underlayer at −0.467 $V_{Ag/AgCl}$ in 0.1 M H_2SO_4 until the total charge passed was 37.9 mC/cm_{geo}^2, which corresponds to a ∼10 nm thick Sn film. Oxidized Sn was deposited onto the Au underlayer by precipitating SnO_2 directly at the electrode surface by controlling the local pH via nitrate reduction to nitrite. The nitrate reduction was performed at −0.6 $V_{Ag/AgCl}$ in 1.5 M HNO_3 until the total charge passed was 3.16 C/cm_{geo}^2, which corresponds to a ∼20 nm thick SnO_2 film. The oxidized Sn film was reductively pretreated at −0.4 V_{RHE} for 5 min in 0.1 M $KHCO_3$ to improve the film's conductivity. Both Sn film deposition procedures used a graphite counter electrode. A non-Pt counter electrode was used during the Au underlayer and Sn film preparation was to avoid Pt dissolution and electrodeposition on the working electrode surface, which can cause erroneous SEIRAS features.[36,37] Once the Sn film was synthesized, spectroscopy was acquired using a Pt counter electrode which only experienced a linear anodic current sweep. Pt dissolution has been shown to be initiated during the oxide reduction process when switching from high anodic potentials back toward cathodic potentials.[38,39] Therefore, the use of a Pt counter electrode should not convolute the SEIRAS features on Sn electrodes. CO_2R experiments were performed on metallic or oxidized Sn electrodes by sparging the electrolyte (0.1 M $KHCO_3$) with CO_2 for 20 min before starting the experiment. Cyclic voltammograms were collected using a Gamry Interface 1010 potentiostat at a sweep rate of 1 mV/s from −0.25 to −1 V_{RHE}. The uncompensated resistance was corrected using the current interrupt compensation feature of the potentiostat. Control experiments were also performed, where the electrolyte was sparged/blanketed with Ar rather than CO_2. All electrochemical experiments were performed using a homemade Ag/AgCl reference electrode, calibrated, and subsequently converted to the RHE potential scale.

Computational Details. GC-DFT calculations were performed using the open-source JDFTx software.[40] The generalized-gradient approximation PBE DFT functional with Grimme's D3 dispersion corrections was used for all calculations.[41,42] The Brillouin zone was sampled using a γ-centered 4 × 4 × 1 folded k-point mesh. The core electrons were modeled with GBRV v1.5 ultrasoft pseudopotentials with an energy cutoff of 20 hartree (544 eV) and a charge density cutoff of 100 hartree (2721 eV).[43] Charge neutrality was ensured by the inclusion of the CANDLE implicit solvation model.[44] The fluid solvent was water with 0.5 M NaF and was chosen as a noninteracting electrolyte. The constant potential calculations were performed by setting the electron chemical potential, μ_{calc}, to the desired potential via eq 1

$$\mu_{calc} = -(V_e + V_{RHE} - 0.059^*pH) \qquad (1)$$

where V_e is the absolute electron potential (taken to be 4.66 eV, calibrated using the CANDLE solvation model[44]), V_{RHE} is
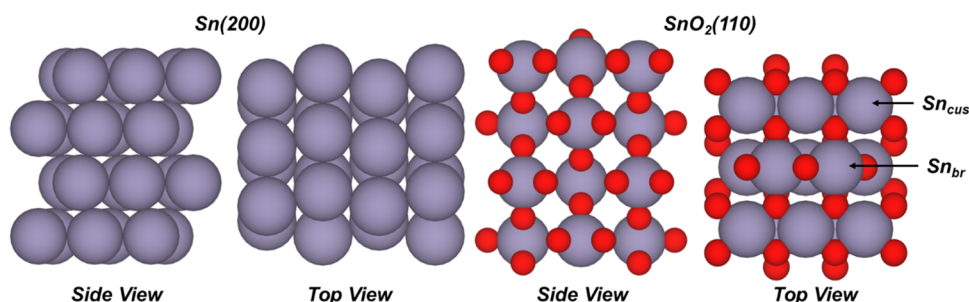
Figure 1. Side and top views of Sn(200) and SnO₂(110) surfaces.

the desired potential on the RHE scale, and pH is the solution pH being modeled. Our calculations were performed at 0, −0.5, and −1 V$_{RHE}$ and a pH of 8 to match the experimental conditions (energies were linearly interpolated between potentials to find equilibrium potentials reported in Results and Discussion). Bulk body-centered tetragonal (bct) Sn and rutile SnO₂ structures, acquired from the Materials Project,[45] were first relaxed and reproduced the experimental lattice parameters within 2% accuracy (calculated a = 5.958 Å, c = 3.157 Å and experimental a = 5.838 Å, c = 3.180 Å for bct Sn;[46] calculated a = 4.811 Å, c = 3.232 Å and experimental a = 4.741 Å, c = 3.187 Å for rutile SnO₂[47,48]). The lowest energy surfaces of each material were taken to be the 200 and 110 surface termination for bct Sn and SnO₂, respectively.[49,50] These surfaces were created using the Pymatgen python package.[51] Both surface unit cells, shown in Figure 1, contained 48 atoms (16 Sn and 32 O atoms for SnO₂(110)), and were 4 atomic layers thick, with at least 30 Å separating the slabs to ensure adequate potential screening. The bottom two atomic layers were frozen to their bulk coordinates. Geometry optimizations were performed using the Atomic Simulation Environment (ASE) python package.[52] Geometry optimizations were considered converged when the net force on the atoms was lower than 0.05 eV/Å. Vibrational frequencies for relevant adsorbates were calculated within JDFTx, with all atoms frozen aside from the adsorbate atoms and surface atoms directly bound to the adsorbate. Grand free energy was calculated according to eq 2

$$\Omega = E_{DFT} - \mu N_e + E_{ZPE} + \int_0^T C_p dT - TS \tag{2}$$

where E_{DFT} is the electronic energy, μ is the potential of the calculation, N_e is the number of electrons in the calculation, E_{ZPE} is the zero-point energy, C_p is the heat capacity, T is the temperature, and S is the total entropy (sum of translational, vibrational, rotational and electronic). For molecules, the free energy corrections were determined from the ideal gas partition function using ASE's thermochemistry IdealGasThermo package. To investigate the vibrational frequency dependence on potential (Stark shift), we also computed the vibrational frequencies (at 298 K) as a function of potential. All converged geometries are shown in Figure S1.

RESULTS AND DISCUSSION

Sn Surface Speciation Under Relevant Electrochemical Conditions. Before examining the thermodynamics of CO₂R intermediates on Sn surfaces, we first evaluated the potential-dependent interactions of both metallic and oxidized Sn with water in the absence of CO₂ across the range of potentials used in experiments. We performed this analysis

because it is commonly claimed that surface hydroxylation is a key element for effective CO₂R catalysis on Sn-based electrodes.[10,13,21] For metallic Sn, we examined the oxidative adsorption of hydroxyl (Sn + OH⁻ → Sn − OH + e⁻) as well as associative adsorption of water molecules. We found that water spontaneously desorbed at all potentials on the Sn(200) surface. Figure 2 shows the coverage of hydroxyls on Sn(200) using a potential-dependent Langmuir adsorption isotherm, shown in eq 3

$$K_{eq,i} = e^{-\Delta\Omega_i(V)/RT}; \; \theta_i = \frac{K_{eq,i}a_i}{1 + K_{eq,i}a_i} \tag{3}$$
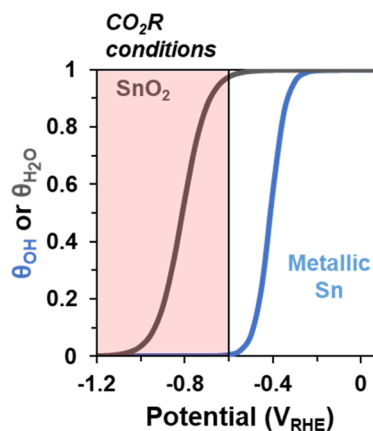

Figure 2. Coverage of OH* on Sn(200) and cus-water on SnO₂(110) as a function of potential, as derived from the potential-dependent change in grand free energy and Langmuir isotherm (eq 3, temperature = 298.15 K, pH = 8 and a_{H_2O} = 1).

The coverage of hydroxyls on Sn(200) approaches zero for potentials more negative than −0.6 V$_{RHE}$. Therefore, for potentials more negative than −0.6 V$_{RHE}$ on fully metallic Sn surfaces, we do not expect surface hydroxyls to make a significant contribution to CO₂R.

Oxidized Sn has a more complex surface speciation, summarized in Figure S2. Stoichiometric metal oxides are known to spontaneously dissociate water to form surface hydroxyls.[53−55] These surface hydroxyls are also known to have different Brønsted acid−base properties, namely that the hydroxyls bound to 5-fold coordinate metal sites (coordinatively unsaturated, or cus-) are more basic than those bound to 6-fold coordinate metal sites (bridge-bound, or br-).[56] We used the stoichiometric SnO₂(110) surface as our model starting point. The results of our calculations agree that stoichiometric SnO₂(110) spontaneously dissociates water to form cus- and
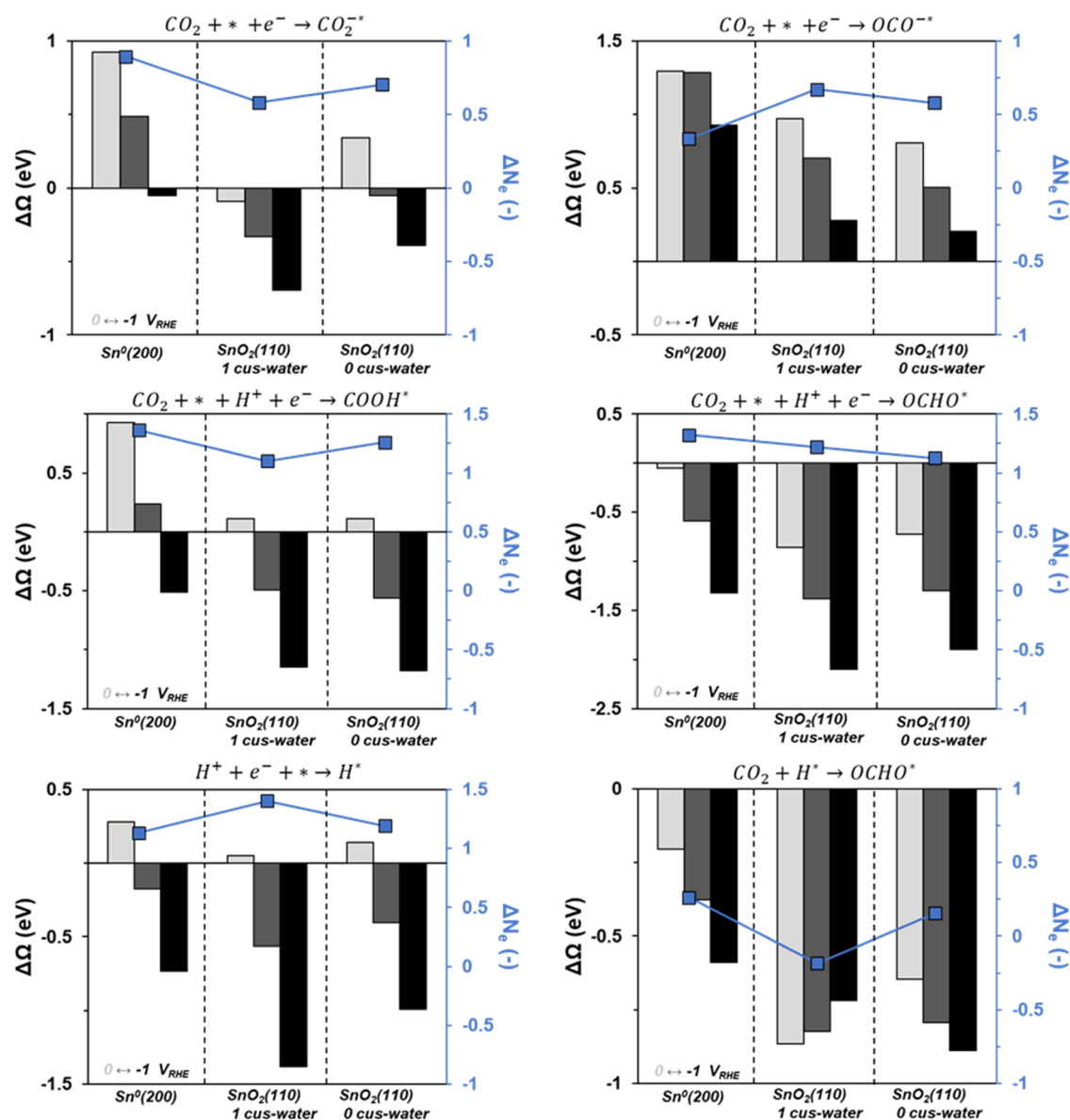
Figure 3. Change in grand free energy as a function of potential for different CO_2 adsorption elementary steps. The potentials are 0 (light gray), -0.5 (dark gray), and -1 (black) V_{RHE}. The reactions represented are reductive adsorption of CO_2 through the carbon atom (top left) and oxygen atom(s) (top right), proton-coupled electron transfer adsorption to form COOH* (middle left) and bidentate OCHO* (middle right), and proton adsorption (bottom left) and CO_2 insertion into a metal-hydride bond to form monodentate OCHO* (bottom right). The average number of electrons transferred across the three potentials is also shown (in blue).

br-hydroxyls at all potentials studied (more positive than -1 V_{RHE}). We also calculated the energy of protonating the cus-hydroxyls and found that, at potentials more negative than -0.5 V_{RHE}, the formation of cus-water groups is also spontaneous. Lastly, we considered the molecular desorption of water from cus- sites and found that it became favorable at potentials more negative than -0.8 V_{RHE}. We found that br-hydroxyls could not be protonated; if a neighboring cus-hydroxyl site was available, the proton was spontaneously transferred to form the more stable cus-water, and if no cus-hydroxyl sites were available, the change in grand free energy was greater than 2 eV at all potentials.

CO_2R on Sn-based electrodes is generally carried out at potentials more negative than -0.5 V_{RHE}, so we considered the starting oxidized surface to be fully hydroxylated/protonated (where all br- sites are br-hydroxyl and all cus- sites are cus-

water). Figure 2 also shows the coverage of cus-water as a function of potential. The coverage remains much higher than fully metallic Sn, only approaching zero at potentials more negative than -1.1 V_{RHE}. Therefore, in the potential regime relevant to CO_2R (-0.5 to -1 V_{RHE}), a non-negligible coverage of cus-water and br-hydroxyl is present. Consequently, we considered the clean Sn(200) (that is, no surface hydroxyls) and a $SnO_2(110)$ surface with partial cus-water coverage (one cus-water and one cus-Sn with two br-hydroxyls), as well as with no cus-water groups (two cus-Sn and two br-hydroxyls). The other consequence of this finding is that a CO_2R mechanism that invokes the formation of surface bicarbonate/carbonate via nucleophilic attack of hydroxyls to CO_2 is unlikely to substantially contribute to the CO_2R activity of Sn-based electrodes.
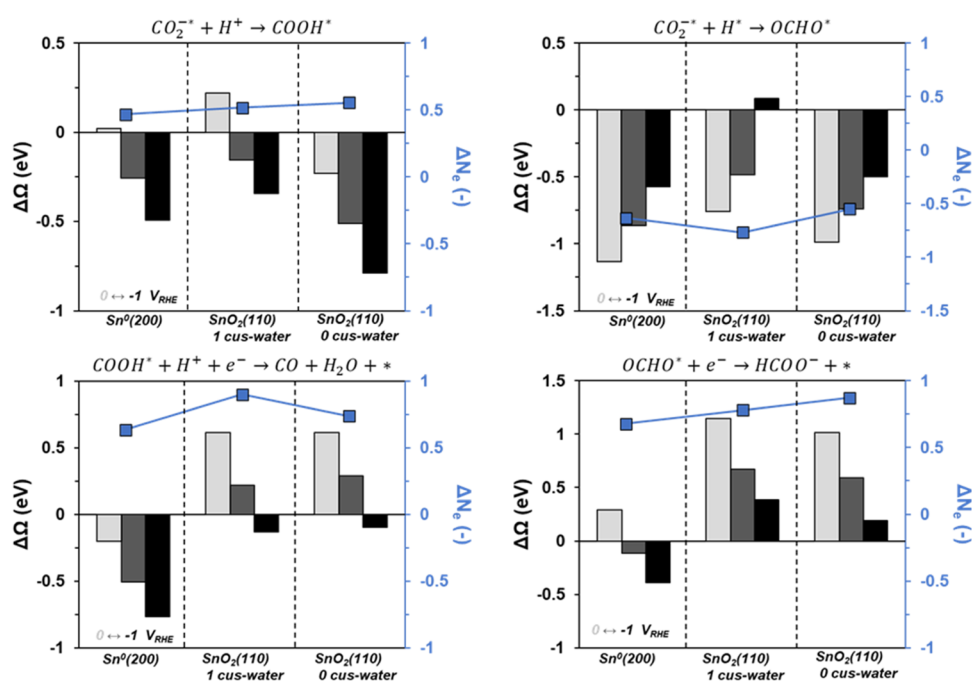
Figure 4. Change in grand free energy as a function of potential for the protonation of $CO_2^{-}*$ (top left), coupling of $CO_2^{-}*$ and H* (top right), reduction of COOH* to form CO (bottom left), and reductive molecular desorption of OCHO* (bottom right). The potentials are 0 (light gray), −0.5 (dark gray), and −1 (black) V_{RHE}. The average number of electrons transferred across the three potentials is also shown (in blue).

Activation of CO_2. It has been proposed that the origin of selectivity toward formate over CO in CO_2R relates to bifurcation in pathways during CO_2 activation. One pathway creates OCHO* adsorbed via surface-oxygen(s) bonds, while the other creates COOH* adsorbed via a surface-carbon bond.[24] However, it is also often proposed that the first elementary step of CO_2R (to either product) is the single-electron reductive adsorption $CO_2 + * + e^- \rightarrow CO_2^{-}*$.[10,13,16,57] The $CO_2^{-}*$ intermediate can be bound through the carbon atom or the oxygen atom(s), which can be protonated to form COOH* or OCHO*, respectively. We therefore considered both the single-electron reductive adsorption and each of the PCET pathways to activate CO_2. We hypothesize that selectivity toward formate originates with the preference of Sn to activate CO_2 through the oxygen atoms rather than the carbon atom. We calculated the adsorption energy of CO_2 in both carbon-bound and oxygen-bound geometries as well as COOH* and OCHO* on the clean metallic Sn(200), SnO_2(110) with 1 cus-water, and SnO_2(110) with no cus-water surfaces as a function of potential, shown in Figure 3. It is immediately apparent however that the selective formation of $OCO^{-}*$ vs $CO_2^{-}*$ is not a reasonable explanation for the selectivity to formate vs CO, on metallic or oxidized Sn, regardless of potential. Reductive adsorption of CO_2 to form $OCO^{-}*$ is not favorable at any potential more positive than −1 V_{RHE}—in fact, CO_2 spontaneously desorbs during geometry optimization at 0 and sometimes −0.5 V_{RHE}, see the Supporting Information, Figures S3 and S4 for a more detailed discussion of this point. In contrast, the formation of $CO_2^{-}*$ becomes favorable at −0.99 and −0.45 V_{RHE} on metallic Sn and SnO_2 with no cus-water, respectively, while the formation of $CO_2^{-}*$ is favorable at all examined potentials on the SnO_2 surface with one cus-water. Therefore, $OCO^{-}*$ is not expected to play a substantial role in CO_2R toward formate. We note that in either case, the number of electrons transferred determined from the GC-DFT is not exactly one, but rather in

the range of 0.4−0.9, depending on the surface and binding geometry. This demonstrates the utility of GC-DFT's ability to determine, rather than assume, the extent of charge transfer.

The formation of OCHO* is more favorable than COOH* across all potentials and surfaces, which is consistent with the experimentally observed selectivity trend. We did not calculate any transition state energies in the current study, and while a large kinetic barrier to forming OCHO* (or COOH*) via the PCET mechanism may exist, we expect the more exothermic step to also possess a lower activation barrier on the basis of Brønsted−Evans−Polanyi (BEP) scaling relationships.[58−60] Once again, we note that the number of electrons transferred in this step is not precisely what would be presumed from writing out the elementary steps, but in this case, more electrons (1.1−1.4) are transferred than expected. The consequence of this asymmetry in the degree of charge transfer is that the PCET adsorption of CO_2 to form either COOH* or OCHO* becomes more favorable at less reducing potentials than the reductive adsorption to form $CO_2^{-}*$.

We also considered the formation of monodentate OCHO* via CO_2 insertion into the Sn−H bond, known as the Eley−Rideal pathway, which has been suggested as a possible pathway for formate-selective CO_2R.[61] Figure 3 (bottom left) shows the energetics for proton reduction for the three different surfaces as a function of potential. The formation of H* becomes favorable at −0.29, 0.26, and −0.12 V_{RHE} on the metallic Sn(200), SnO_2(110) with one cus-water, and SnO_2(110) with zero cus-water surfaces, respectively. Therefore, under potentials relevant for CO_2R, we expect a non-negligible coverage of H*, especially considering the adsorption energy is more favorable than for the adsorption of $CO_2^{-}*$. Figure 3 (bottom right) shows the energetics for insertion of CO_2 into the Sn−H bond. For all surfaces at all potentials, the formation of OCHO* in this fashion is favorable. There is less than a 0.1 eV difference in the formation energy for monodentate OCHO* and bidentate
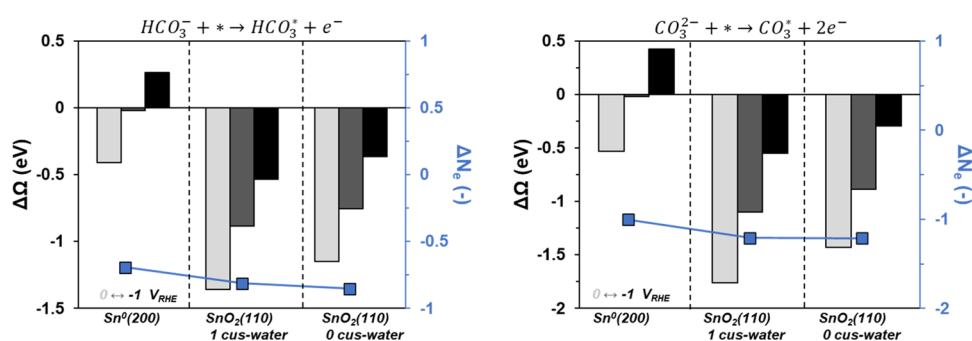
Figure 5. Change in grand free energy as a function of potential for the molecular adsorption of bicarbonate (left) and carbonate (right). The potentials are 0 (light gray), −0.5 (dark gray), and −1 (black) V_{RHE}. The average number of electrons transferred across the three potentials is shown (in blue).

OCHO*. The potential dependence of the energetics of CO_2 insertion into the Sn–H bond is attenuated when compared to the Faradaic reactions in the other panels of Figure 3 because there is a lower, near-zero amount of electron transfer involved in this reaction, i.e., this is a chemical step. The origin of the potential dependence of this step may be due to second-order effects such as the interaction of the adsorbate dipole with the developing electric field, or changes in the stabilization of the electrolyte due to changes in the local concentration of electrolyte ions.[62]

Formation of Desorbed CO and Formate. The previous section compared the different pathways CO_2 may take to form an activated adsorbate on the surface of Sn-based catalysts. We now consider the next steps of CO_2R that involve the desorption of the products CO and formate. We started by calculating the adsorbate geometry of both CO and formic acid on the three Sn surfaces but found that they do not adsorb under any conditions considered (Figures S5 and S6). Therefore, moving forward we assume that any step that forms either CO or formic acid includes spontaneous desorption.

First, we considered reactions involving CO_2^{-}*. We note that the energetics presented in the previous section do not rule out the formation of CO_2^{-}* simply because the PCET adsorption to form COOH* or OCHO* is more downhill. The presence of a large kinetic barrier for the PCET steps and sufficiently low barrier for the direct reductive adsorption of CO_2^{-}* could lead to non-negligible flux through this pathway, particularly on the oxide surfaces which bind CO_2^{-}* more strongly than metallic Sn. Both COOH* and OCHO* are accessible from CO_2^{-}*, the former likely coming from a proton transfer and the latter likely coming from a surface-catalyzed coupling of CO_2^{-}* with H*. The energetics for these reactions are depicted in Figure 4. Protonation of CO_2^{-}* is not purely a proton transfer—the GC-DFT calculation predicts that ~0.5 electrons are transferred during this step as well. The formation of COOH* in this manner is mostly favorable across the three surfaces at all potentials considered. The Langmuir–Hinshelwood coupling between H* and CO_2^{-}* to form OCHO* is also mostly favorable across all potentials and surfaces studied, although interestingly the calculated electron transfer shows that this is an oxidation, with ~0.5 electrons transferred to, rather than from, the electrode. This step therefore becomes less favorable with more negative potential.

Next, we consider the reactions that form the CO or desorbed formate products (Figure 4). We examined a PCET reduction of COOH* to form CO and water as the pathway to

CO and the reductive molecular desorption of OCHO* as the primary pathway to formate. We also considered the Langmuir–Hinshelwood coupling of COOH* and H* to form formic acid directly, but due to a less favorable change in grand free energy that becomes increasingly less favorable at more negative potential than the direct desorption, we do not consider it to be an active pathway (Figure S7). Interestingly, metallic Sn has a much larger driving force to form CO than either of the oxide surfaces, which only become favorable at potentials more negative than −0.8 V_{RHE}. This is somewhat expected based on the observation that COOH* is bound less strongly on the metallic Sn surface than on the SnO_2 surfaces. The same trend is observed when considering the reductive molecular desorption of OCHO*, where the desorption is more favorable on the metallic surface than the oxide. Without explicit calculation of transition state energetics, we cannot definitively say which of these steps will be kinetically faster, but molecular adsorption/desorption steps typically do not have significant activation barriers. Complex reaction coordinates such as reducing COOH* to CO and water may have an appreciable activation barrier, so the reductive desorption of OCHO* and formation of CO may be relatively competitive in rate.

Competition by HER and Carbonate Adsorption. The competition between cathodic reactions and HER is ubiquitous in electrocatalysis. An additional parasitic reaction that can lower the efficiency of CO_2R is the strong adsorption of bicarbonate and carbonate, which are present in CO_2R electrochemical cells either as supporting electrolyte or formed spontaneously from the equilibrium of CO_2 and water/hydroxide. To holistically evaluate the performance of metallic and oxidized Sn catalysts for CO_2R, we also considered the competition from HER and bicarbonate/carbonate adsorption.

HER may follow two well-known mechanisms: the Volmer–Heyrovsky and Volmer–Tafel mechanisms.[63] HER on Sn is thought to mainly follow the Volmer–Heyrovsky mechanism due to low coverage of H* until larger overpotentials, by which time the rate of the Heyrovsky step becomes fast enough to scavenge H*.[64] We consider both mechanisms for the sake of completeness. Figure S8 shows the reaction coordinate diagrams for both the Volmer–Heyrovsky and Volmer–Tafel mechanisms on all three surfaces as a function of applied potential. The results agree with the existing literature that the Volmer–Heyrovsky mechanism is preferred on all Sn surfaces, with all steps being thermodynamically downhill at potentials more negative than −0.3 V_{RHE}. The presence of a large kinetic barrier for the Heyrovsky step could lead to non-negligible flux

through the Volmer−Tafel mechanism on metallic Sn once an appreciable coverage of H* has accumulated. Each Volmer step transfers 1.1−1.4 electrons from the electrode, meaning that 0.2−0.8 electrons must be transferred back to the electrode during the Tafel step. Therefore, the Tafel step becomes less favorable at more negative potentials. This is more pronounced on the SnO_2 surfaces, so it is even more likely that the reaction proceeds through the Volmer−Heyrovsky mechanism on these surfaces. The most significant consequence of this is that, because the Volmer step is potential-determining on all three surfaces (for the Volmer−Heyrovsky mechanism), the surface coverage of H* is likely to be low (but not zero) because of the favorable reaction between either H^+ to from H_2 or CO_2 to form OCHO*. This will negatively impact the rate of CO_2R steps that involve H* unless there is a much lower kinetic barrier for these steps than the Heyrovsky step.

Next, we considered the competitive adsorption of bicarbonate/carbonate. Bicarbonate is often the supporting electrolyte of choice for CO_2R because it can retard the aqueous CO_2 equilibrium, which results in efficiency losses.[65,66] This aqueous CO_2 equilibrium means that bicarbonate will likely be present even in electrolytes that do not have intentionally added bicarbonate and therefore must be considered when evaluating the surface processes of CO_2R catalysts. Lastly, carbonate may begin to accumulate near the electrode interface due to the increase in pH that arises from the consumption of protons during cathodic reactions.[67] It is not unusual for the interfacial pH of a cathode to be 2−4 pH units higher than the bulk pH, meaning the interfacial pH could be greater than the pK_a of bicarbonate.[68] Figure 5 shows the energetics for the molecular adsorption of bicarbonate and carbonate on the three Sn surfaces as a function of potential. In line with the results described above for all previously discussed adsorbates, metallic Sn binds both bicarbonate and carbonate more weakly than either of the SnO_2 surfaces. The adsorption of bicarbonate and carbonate becomes less favorable at more negative potentials as expected due to the net oxidation during adsorption. The net electrons transferred for bicarbonate is close to the expected value of 1, but the number of electrons transferred for carbonate is much lower than the expected value of 2, only slightly above 1. This means the carbonate adsorbate is partially charged and the adsorption energy is less sensitive to potential than expected. We also considered the energetics of the adsorption of bicarbonate with a simultaneous discharge of its proton to form adsorbed carbonate (Figure S9), but this process was less favorable than either of the two molecular adsorption processes and is therefore not expected to contribute significantly to the adsorption processes. This evidence suggests that molecular adsorption of bicarbonate and carbonate can compete with other intermediates for active sites at low potential, but will be driven off of the surface at more negative potentials.

Before discussing the results of the ATR-SEIRAS experiments, we summarize the observations from the preceding sections. First, metallic Sn is unlikely to have an appreciable coverage of hydroxyls during CO_2R, whereas oxidized Sn may have a non-negligible coverage of hydroxyls and water groups throughout the CO_2R relevant potential window. Next, CO_2 has four feasible activation pathways: direct reductive adsorption to form CO_2^-* bound through the carbon atoms, PCET adsorption to form either COOH* or OCHO*, and insertion of CO_2 into a Sn−H bond to form OCHO*. CO_2^-*

can subsequently be protonated to form COOH*, which may react to form CO and H_2O in a final PCET, or react with H* to form OCHO*, which subsequently undergoes reductive molecular desorption to form solution-phase formate. A non-negligible competition may exist between CO_2R and (i) molecular adsorption of bicarbonate/carbonate at low over-potential and (ii) Volmer−Heyrovsky HER at higher over-potential.

ATR-SEIRAS on Metallic and Oxide-Derived Sn. With some degree of understanding of what might be present on the surface during CO_2R from the GC-DFT analysis described above, we performed ATR-SEIRAS experiments to validate and refine this understanding. We previously reported a method to prepare both fully metallic and oxidized SEIRAS-active Sn films, which we used in the present study to discern differences in adsorbed species during CO_2R.[32] Before we begin the discussion of the SEIRAS results, we would like to point out that ex situ characterization of the two Sn films after the reductive treatment shows that they have similar degrees of oxidation. Both Sn films undergo spontaneous oxidation in air, which complicates the assignment of the exact oxidation state of the two films during CO_2R. Dutta et al. performed operando EXAFS experiments on SnO_2-based catalysts and found that metallic Sn coordination was not observed until −0.88 V_{RHE}, and SnO_2 and SnO features were still observed even at −1 V_{RHE}.[18] Therefore, while the oxidized Sn film undoubtedly partially reduces under the electrochemical conditions present in CO_2R, we do not necessarily expect it to resemble the fully metallic Sn film under the conditions examined and spectroscopic differences between the two Sn films may still appear. Figure 6 shows the ATR-SEIRAS spectra for both the metallic and oxidized Sn film as a function of potential during CO_2R. We point out two common features for both samples, at ~1200 and ~1100 cm^{-1}. These features are attributed to the Si(100) phonon that comes from the wafer used to perform the ATR-SEIRAS experiment.[69] There may also be trace amounts of sulfate that remain from the electrosynthesis of the Sn films. Both features are present during blank experiments with no CO_2 or bicarbonate present and will not be discussed or interpreted further. The observed vibrational frequencies are collected in Table 1.

First, we observe positive bands in the 3200−3500 cm^{-1} region that could be assigned to changes in the interfacial water structure during electrode polarization.[70,71] The band at 1611 and 1635 cm^{-1} for metallic and oxidized Sn, respectively, is likely also related to changes in interfacial water structure. A difference between the two materials is seen in the high-frequency O−H stretch region, where metallic Sn has a negative band at 3562 cm^{-1} and oxidized Sn has a positive band at 3644 cm^{-1}. Given that the calculated PZC for Sn(200) is −0.52 V_{RHE} and the onset of the negative band is at −0.6 V_{RHE}, the O−H stretches might be attributed to shifts in the interfacial water structure. However, these high-frequency spectral features have also previously been assigned to "dangling" surface hydroxyls that have less hydrogen bonding than water.[56] Given that GC-DFT predicts that hydroxyls will desorb from metallic Sn at a similar potential, the negative IR peak is also consistent with the desorption of surface hydroxyls. This also explains why no such negative peak appears for the oxidized Sn surface, where the cus-hydroxyls spontaneously form cus-water, and br-hydroxyls are not predicted to desorb at these potentials. Furthermore, the negative IR peak is fully reversible, which implies that as the potential is returned to the
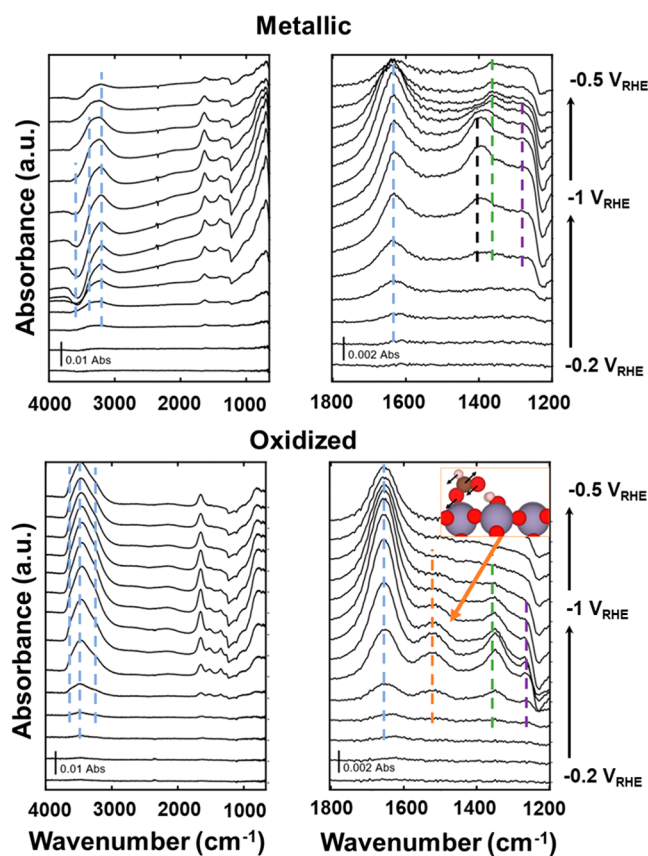
Figure 6. Full (4000−800 cm^{-1}, top left) and carbonaceous region (1800−1200 cm^{-1}, top right) ATR-SEIRAS spectra on the metallic Sn electrode during CO_2R. Full (4000−800 cm^{-1}, bottom left) and carbonaceous region (1800−1200 cm^{-1}, bottom right) ATR-SEIRAS spectra on the oxidized Sn electrode during CO_2R. Colored lines are drawn to guide the eye (spectra without these lines are available in the Supporting Information, Figures S34 and S35). Conditions: 0.1 M $KHCO_3$ (pH = 8) with bubbling CO_2, Sn, or SnO_x thin-film deposited on Au working electrode, Pt wire counter electrode and Ag/AgCl reference electrode. Inset: monodentate formate adsorbed on $SnO_2(110)$ with no cus-waters with annotated vibration vectors for the calculated vibrational frequency of 1519 cm^{-1}.

Table 1. Observed Vibrational Frequencies (in cm^{-1}) for the Metallic and Oxidized Sn Films from Figure 6, along with the Corresponding Assignments

metallic Sn		oxidized Sn	
frequency (cm^{-1})	assignment	frequency (cm^{-1})	assignment
3562 (loss)	desorption of OH*	3644	interfacial water
3366	interfacial water	3486	interfacial water
3209	interfacial water	3256	interfacial water
~2400 (loss)	consumption of CO_2	~2400 (loss)	consumption of CO_2
1611	interfacial water	1635	interfacial water
1410	solution-phase carbonate	1524	monodentate formate
1363	monodentate formate	1349	monodentate formate
1282	monodentate formate	1267	monodentate formate

starting value, the vibrating species can return to their prior state.

Focusing now on the bands that may be associated with carbon-bearing species, both the metallic and oxidized Sn materials have loss bands at ~2400 cm^{-1} that appear between −0.5 and −0.6 V$_{RHE}$ (although it is more apparent on the metallic Sn surface). These bands can be assigned to the consumption of CO_2 during electrolysis. However, it is not immediately obvious if this is simply due to the reactions of CO_2R, or if some of the CO_2 is converted to aqueous bicarbonate and carbonate at the electrode interface due to the cathodic pH increase. We refrain from interpreting the magnitude of these bands because of this ambiguity. Next, there is a band at 1524 cm^{-1} that is only present on the oxidized Sn surface and grows between −0.5 and −0.6 V$_{RHE}$, before mostly decreasing to the background level. A peak in this region has previously been interpreted as formate,[72] bicarbonate[21] and carbonate,[10] so we attempted to assign this band by calculating the vibrational frequencies. Table S1 shows the GC-DFT-calculated vibrational frequencies as a function of potential for the Sn(200), $SnO_2(110)$ with 1 cus-water, and $SnO_2(110)$ with no cus-waters. For the oxidized Sn surfaces, the observed vibrational frequency is most consistent with monodentate formate and bidentate bicarbonate adsorbates. However, due to the surface selection rule, only adsorbate vibrational modes with a change in dipole that is perpendicular to the surface will be IR active. Visualizations of the vibrational modes are provided in Figures S10−S33 (gif file animations are also available in the Supporting Information). For both monodentate formate and bidentate bicarbonate, the vibrational mode responsible for the frequency that is closest to the observed value is the OCO asymmetric stretch. The vibration coordinate, shown as an inset in Figure 6, is more perpendicular for monodentate formate than for bidentate bicarbonate, so we assign this peak as monodentate formate. An additional clue that this is less likely to be bicarbonate and more likely to be formate is that we predicted the formation of formate to become increasingly favorable and the adsorption of bicarbonate to become decreasingly favorable at more negative potentials. Monodentate formate was assigned to a feature at 1680 cm^{-1} by Jiang et al. when studying CO_2R on Pd-based electrocatalysts.[72] They also assigned a peak at 1584 cm^{-1} to solution-phase, desorbed formate. This peak position differs significantly from both what we have observed in our own spectra and calculated using GC-DFT, but the difference could be explained by both differences in vibrational frequencies across different materials and under different electrochemical environments.

The next peak observed and used for mechanistic analysis is only present in the metallic Sn catalyst spectra as a reversible peak that appears at 1410 cm^{-1} at potentials more negative than −0.6 V$_{RHE}$. This feature is most consistent with either monodentate carbonate, or solution-phase carbonate which would arise from the increase in interfacial pH. GC-DFT calculations predict that carbonate will desorb from metallic Sn at these potentials, so it is more likely that solution-phase carbonate has accumulated at the electrode interface. The absence of this feature in the oxidized Sn spectra is of particular interest, as the I−V curves (Figure S36) show that oxidized Sn draws a higher current (as well as higher current density) than metallic Sn, which implies that the consumption of protons at the interface should be higher on oxidized Sn than metallic Sn. This may be explained by the presence of the cus-water and br-hydroxyl groups on the oxidized Sn surface playing a buffering role, that is, when solution-phase protons
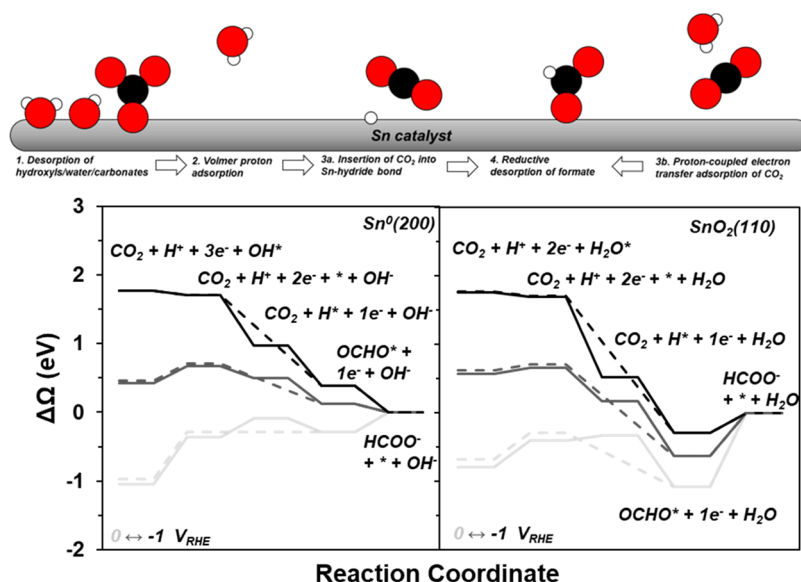
Figure 7. (Top) Schematic visualizing the proposed mechanism in Mechanism 1 and reaction coordinate diagram for metallic Sn (bottom left) and the average between oxidized Sn with one and no cus-waters (bottom right) for the proposed mechanism in Mechanism 1. The solid lines are for the Eley−Rideal pathway, and the dashed lines are for the PCET pathway.

are consumed in cathodic reactions, protons on the surface may be released to neutralize the change at the interface. To evaluate the feasibility of this hypothesis, we determined the favorability of transferring a proton from the $SnO_2(110)$ surface to a carbonate ion (Figure S37), which was favorable at all potentials. Therefore, a complex equilibrium exists at the interface of the oxidized Sn surface that may be able to neutralize the expected pH increase upon cathodic polarization. Metallic Sn is unable to perform this interfacial buffering because its surface hydroxyls have been reduced off the surface at these potentials. Assigning the relative importance of the intrinsic electrode reactivity and the local pH on the activity and selectivity of Sn-based CO_2R catalysis would require a sophisticated coupled transport-kinetic model like Singh et al. developed for CO_2R on Ag catalysts.[4] Cao et al. assigned this feature to monodentate formate in their investigation of CO_2R to formate over two-dimensional Bi catalysts.[73] They measured this peak in the absence of CO_2 without quantifying or detecting any formate production, so it is more likely that this peak is also due to the formation of carbonate once the pH increases from the cathodic consumption of protons.

The remaining bands, at 1363/1282 and 1349/1267 cm^{-1} for metallic and oxidized Sn, respectively, likely belong to monodentate formate. This is consistent with the calculated vibrational frequencies from GC-DFT for both surfaces. The peaks at 1363 and 1349 cm^{-1} are assigned to the combination mode of C−H wagging and OCO bending, and the peaks at 1282 and 1267 cm^{-1} are assigned to the OCO symmetric stretch. As with the formate peak at 1524 cm^{-1}, this assignment is strengthened by the reversible appearance of these features at potentials more negative than −0.6 V_{RHE}. One difference between the metallic and oxidized Sn spectra is that the peak at 1363 cm^{-1} is not fully reversible on metallic Sn, and a small peak is still present at −0.5 V_{RHE} on the backsweep. We assign this as readsorbed formate, but the GC-DFT calculations predict that formate is bound more strongly to oxidized Sn than metallic, so we expected that this feature would be present in the oxidized case too. However, there is
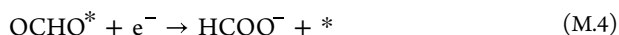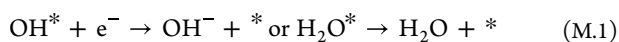
also a larger driving force to readsorb hydroxyls at more positive potentials on oxidized Sn. Therefore, because a much weaker driving force exists for hydroxyl adsorption on metallic Sn, formate may only be displaced from metallic Sn at more positive potentials.

Finally, to assist with the assignments of the features in Figure 6, we repeated the SEIRAS experiment without CO_2 present in the electrochemical cell. Figure S38 (nonannotated versions in Figures S39 and S40) shows the SEIRAS spectra for both the metallic and oxidized Sn materials. For the metallic Sn electrode, only the signals corresponding to the changes in interfacial water and the solution-phase carbonate persist in the absence of CO_2. The solution-phase carbonate arises due to the pH increase from HER. This supports the assignment of the other peaks at 1363 and 1282 cm^{-1} as formate (or at least intermediates from CO_2R) and not molecular adsorption of bicarbonate/carbonate present in the electrolyte. Similarly, most of the SEIRAS features disappear for the oxidized Sn electrode when CO_2 is removed from the electrolyte. The features that arise from changes in the interfacial water remain, and a new negative feature appears at 1450 cm^{-1}. This peak is most consistent with bidentate carbonate. This shows that there may be carbonate adsorption from the electrolyte on the oxidized Sn surface that can be reduced off of the surface, which is supported by the results of calculations reported in Figure 5. The disappearance of the peaks at 1524, 1349, and 1267 cm^{-1} when CO_2 is absent confirms that these peaks originate from CO_2R intermediates that are most likely monodentate formate.

Proposed Mechanism and Strategies for Improved CO_2R. Through both the GC-DFT and ATR-SEIRAS analyses described above, we have identified CO_2R pathways that are feasible on both metallic and oxidized Sn surfaces. For metallic Sn, surface hydroxyls are reductively desorbed by −0.6 V_{RHE} (M.1). Direct reductive adsorption of CO_2 to form OCO^-* does not become favorable until potentials more negative than −1 V_{RHE}, which is more negative than the observed onset of peaks assigned to formate in the ATR-SEIRAS spectra. Therefore, we believe that CO_2 is activated either by insertion

into the Sn−H bond via an Eley−Rideal-like step (M.3a), preceded by Volmer proton adsorption (M.2), or PCET adsorption to OCHO* (M.3b). Only monodentate formate was detected using ATR-SEIRAS, which supports the Eley−Rideal activation of CO_2 on metallic Sn because there is a larger driving force for formate desorption than to rearrange into the bidentate configuration. Jiang et al. made a similar conclusion regarding the formation of monodentate formate when investigating CO_2R on Pd-based catalysts.[72] The potential limiting step for this mechanism is the reductive molecular desorption of formate (M.4), which becomes favorable at −0.39 V_{RHE}. The lack of IR bands associated with formate at this potential on metallic Sn is explained by the presence of hydroxyls, which are not predicted to completely vacate the surface until −0.6 V_{RHE}. This mechanism is summarized in Mechanism 1 and Figure 7, which also shows the free energy landscape for the pathways on metallic and oxidized Sn.

Mechanism 1. Proposed mechanism for CO_2R to formate on Sn-based catalysts

$$OH^* + e^- \rightarrow OH^- + {}^* \text{ or } H_2O^* \rightarrow H_2O + {}^* \tag{M.1}$$

$$H^+ + e^- + {}^* \rightarrow H^* \tag{M.2}$$

$$CO_2 + H^* \rightarrow OCHO^* \tag{M.3a}$$

$$CO_2 + H^+ + e^- + {}^* \rightarrow OCHO^* \tag{M.3b}$$

$$OCHO^* + e^- \rightarrow HCOO^- + {}^* \tag{M.4}$$

For oxidized Sn, the mechanism is more similar to metallic Sn than expected based on the differences in the energetics predicted from GC-DFT. The surface is initially blocked by cus-water groups that begin to desorb at −0.6 V_{RHE} (M.1). Next, because the oxidized Sn surface has higher affinity for all intermediates than metallic Sn, it is possible that all of the proposed CO_2 activation pathways are accessible. However, unless there are substantial kinetic barriers for all of the steps except direct reductive adsorption of CO_2, there is a larger driving force to form H*, COOH*, and OCHO* at potentials more negative than −0.5 V_{RHE} due to the greater extent of charge transfer. We expect that any COOH* formed will go on to produce CO, so the same two CO_2 activation steps (Eley−Rideal reaction between CO_2 and H* and PCET adsorption to form OCHO*) are most likely. Desorption of formate is again the potential-determining step, although for oxidized Sn it is predicted to be −1.22 V_{RHE}. This implies that the active phase of Sn during CO_2R is likely a partially reduced Sn oxide (or partially oxidized metallic Sn) such that the energetics of both activation and desorption steps are in between the two limiting cases examined in this study. We also considered the hydroxyl-mediated pathway proposed by Baruch et al.,[21] and cannot conclusively eliminate it as a possibility but believe that is likely only a minor contribution to the overall CO_2R rate (see the Supporting Information and Figures S41−S43). Metallic and oxidized Sn surfaces having different rate-limiting steps should manifest as different Tafel slopes. The electrochemical cell used for the SEIRAS experiments is not equipped to accurately determine the Tafel slope for CO_2R toward formate due to influences from mass transport and very low product concentrations, so more thorough kinetic measurements to determine the reaction orders, apparent activation barriers and the Tafel slope under a broader range of conditions will be necessary to fully resolve the mechanistic differences between metallic and oxidized Sn electrocatalysts.

The proposed mechanism, and data that lead to it, highlight the factors that limit CO_2R on Sn. On either metallic or oxidized Sn, GC-DFT predicts that the electrochemical activation of CO_2 becomes favorable at a less negative potential than the observed onset potential of −0.6 V_{RHE}, which coincides with the potential at which hydroxyls or molecular water groups are predicted to desorb from the surfaces. Therefore, lowering the overpotential of CO_2R on Sn will require decreasing the affinity of Sn surfaces toward hydroxyls/water. Doing so will be challenging to achieve because, due to adsorbate scaling relationships, surfaces that bind one class of adsorbates more weakly typically bind all classes of adsorbates more weakly, and as such lowering the potential for hydroxyl/water removal will also increase the potential for CO_2 activation. Some strategies for decorrelating carbon-bound and oxygen-bound adsorbates have been proposed, such as alloying with distinct elements such as sulfur and taking advantage of interfaces between different materials like RuO_2 and CeO_2.[15,74−77] Controlling the near-electrode environment could also be a beneficial strategy. It has been demonstrated that the presence of electrolyte additives, such as self-assembled monolayers[70,71] and ionomer coatings[78] can modify the hydrophilicity of the electrode interface. Selectively destabilizing surface hydroxyls/water in this manner could lower the overpotential required to open active sites for CO_2R on Sn surfaces.

CONCLUSIONS

In this study, we used GC-DFT and ATR-SEIRAS to interrogate the differences in CO_2R mechanism toward formate on both metallic and oxidized Sn surfaces. While the computed energetics and observed IR features are distinct for both materials, we have proposed probable mechanistic steps that are common to both materials, with different limiting characteristics. The steps most consistent with our study are 1. Potential-driven desorption of hydroxyls/water/bicarbonate, 2. Volmer proton adsorption, 3a. Eley−Rideal insertion of CO_2 into a Sn−H bond, 3b. PCET adsorption of CO_2, and 4. Reductive desorption of formate. Metallic Sn is less likely to be limited by the desorption of formate or other spectator species such as bicarbonate, carbonate, and hydroxyls, but oxidized Sn is more able to facilely activate CO_2. In both cases, hydroxyls and molecular water must be driven off the surface to open active sites for CO_2R. This analysis ultimately supports the conclusion that Sn surfaces are in situ oxidized or reduced to achieve an intermediate oxidation state such as Sn_2O_3 or SnO, that is more optimally active for the CO_2R to formate than fully metallic or oxidized Sn. Future investigations of Sn-based electrocatalysts should focus on (1) Identifying the exact speciation of the operando Sn catalyst, (2) Calculating the explicit activation energies of the elementary steps identified here as most relevant and (3) Experimentally determining the kinetic signatures like reaction orders, apparent activation barriers, and apparent transfer coefficients across a diverse set of experimental conditions to diagnose the mechanism with more confidence.

ASSOCIATED CONTENT

Ⓢ Supporting Information

The Supporting Information is available free of charge at https://pubs.acs.org/doi/10.1021/acscatal.4c01290.

GC-DFT calculated adsorption geometries; discussion of $SnO_2(110)$ surface speciation; additional discussion of GC-DFT for computational electrochemistry; additional discussion of CO_2R adsorption intermediates; discussion of hydroxyl-mediated CO_2R pathway on SnO_2; hydrogen evolution reaction energetics; SEIRAS spectra of Ar-saturated experiments; nonannotated SEIRAS spectra; cyclic voltammograms corresponding to SEIRAS experiments; visualization of calculated vibrations; and tabulation of calculated vibrational frequencies (PDF)

Animations of the calculated vibrations as .gif files (ZIP)

◼ AUTHOR INFORMATION

Corresponding Authors

Wilson A. Smith − *Department of Chemical and Biological Engineering, Renewable and Sustainable Energy Institute, University of Colorado Boulder, Boulder, Colorado 80303, United States; National Renewable Energy Laboratory, Golden, Colorado 80401, United States;* ⓘ orcid.org/0000-0001-7757-5281; Email: Wilson.Smith@nrel.gov

Derek Vigil-Fowler − *National Renewable Energy Laboratory, Golden, Colorado 80401, United States; Materials, Chemical, and Computational Science Directorate, National Renewable Energy Laboratory, Golden, Colorado 80401, United States;* Email: Derek.Vigil-Fowler@nrel.gov

Authors

Todd N. Whittaker − *Department of Chemical and Biological Engineering, Renewable and Sustainable Energy Institute, University of Colorado Boulder, Boulder, Colorado 80303, United States;* ⓘ orcid.org/0000-0001-8565-5396

Yuval Fishler − *Department of Chemical and Biological Engineering, Renewable and Sustainable Energy Institute, University of Colorado Boulder, Boulder, Colorado 80303, United States;* ⓘ orcid.org/0000-0001-7764-9455

Jacob M. Clary − *National Renewable Energy Laboratory, Golden, Colorado 80401, United States; Materials, Chemical, and Computational Science Directorate, National Renewable Energy Laboratory, Golden, Colorado 80401, United States;* ⓘ orcid.org/0000-0002-6144-759X

Paige Brimley − *Department of Chemical and Biological Engineering, Renewable and Sustainable Energy Institute, University of Colorado Boulder, Boulder, Colorado 80303, United States;* ⓘ orcid.org/0000-0002-9064-922X

Adam Holewinski − *Department of Chemical and Biological Engineering, Renewable and Sustainable Energy Institute, University of Colorado Boulder, Boulder, Colorado 80303, United States;* ⓘ orcid.org/0000-0001-8307-5881

Charles B. Musgrave − *Department of Chemical and Biological Engineering, Renewable and Sustainable Energy Institute, University of Colorado Boulder, Boulder, Colorado 80303, United States; Materials Science and Engineering Program, University of Colorado Boulder, Boulder, Colorado 80303, United States;* ⓘ orcid.org/0000-0002-5732-3180

Carrie A. Farberow − *National Renewable Energy Laboratory, Golden, Colorado 80401, United States; Catalytic Carbon Transformation and Scale-Up Center, National Renewable Energy Laboratory, Golden, Colorado 80401, United States*

Complete contact information is available at:
https://pubs.acs.org/10.1021/acscatal.4c01290

Author Contributions

D.V.−F., W.A.S., and T.N.W. conceived the project. T.N.W. ran all GC-DFT calculations. Y.F. ran all SEIRAS experiments. T.N.W. and Y.F. analyzed the data and created the figures. T.N.W. drafted the manuscript. All authors reviewed and edited the manuscript.

Notes

The authors declare no competing financial interest.

◼ REFERENCES

(1) Overa, S.; Ko, B. H.; Zhao, Y.; Jiao, F. Electrochemical Approaches for CO2 Conversion to Chemicals: A Journey toward Practical Applications. *Acc. Chem. Res.* **2022**, *55*, 638−648, DOI: 10.1021/acs.accounts.1c00674.

(2) Nitopi, S.; Bertheussen, E.; Scott, S. B.; Liu, X.; Engstfeld, A. K.; Horch, S.; Seger, B.; Stephens, I. E. L.; Chan, K.; Hahn, C.; Nørskov, J. K.; Jaramillo, T. F.; Chorkendorff, I. Progress and Perspectives of Electrochemical CO2 Reduction on Copper in Aqueous Electrolyte. *Chem. Rev.* **2019**, *119* (12), 7610−7672.

(3) Monteiro, M. C. O.; Philips, M. F.; Schouten, K. J. P.; Koper, M. T. M. Efficiency and Selectivity of CO2 Reduction to CO on Gold Gas Diffusion Electrodes in Acidic Media. *Nat. Commun.* **2021**, *12* (1), No. 4943.

(4) Singh, M. R.; Goodpaster, J. D.; Weber, A. Z.; Head-Gordon, M.; Bell, A. T. Mechanistic Insights into Electrochemical Reduction of CO2 over Ag Using Density Functional Theory and Transport Models. *Proc. Natl. Acad. Sci. U.S.A.* **2017**, *114* (42), E8812−E8821.

(5) Somoza-Tornos, A.; Guerra, O. J.; Crow, A. M.; Smith, W. A.; Hodge, B.-M. Process Modeling, Techno-Economic Assessment, and Life Cycle Assessment of the Electrochemical Reduction of CO2: A Review. *iScience* **2021**, *24* (7), No. 102813.

(6) Hietala, J.; Vuori, A.; Johnsson, P.; Pollari, I.; Reutemann, W.; Kieczka, H. Formic Acid. In *Ullmann's Encyclopedia of Industrial Chemistry*, 7th ed.; Wiley-VCH Verlag GmbH & Co: Hoboken, NJ, 2016; Vol. *A12*, pp 1−22.

(7) Pourbaix, M. *Atlas of Electrochemical Equilibria in Aqueous Solutions*; Pergamon Press: Oxford; New York, 1966.

(8) Lide, D. R. *CRC Handbook of Chemistry and Physics*, 84th ed.; Taylor & Francis, 2003.

(9) He, M.; Xu, B.; Lu, Q. Probing the Role of Surface Speciation of Tin Oxide and Tin Catalysts on CO2 Electroreduction Combining in

Situ Raman Spectroscopy and Reactivity Investigations. *Chin. J. Catal.* **2022**, *43* (6), 1473−1477.

(10) Deng, W.; Zhang, L.; Li, L.; Chen, S.; Hu, C.; Zhao, Z.-J.; Wang, T.; Gong, J. Crucial Role of Surface Hydroxyls on the Activity and Stability in Electrochemical CO2 Reduction. *J. Am. Chem. Soc.* **2019**, *141* (7), 2911−2915.

(11) Chen, Y.; Vise, A.; Klein, W. E.; Cetinbas, F. C.; Myers, D. J.; Smith, W. A.; Deutsch, T. G.; Neyerlin, K. C. A Robust, Scalable Platform for the Electrochemical Conversion of CO2 to Formate: Identifying Pathways to Higher Energy Efficiencies. *ACS Energy Lett.* **2020**, *5* (6), 1825−1833.

(12) Hu, L.; Wrubel, J. A.; Baez-Cotto, C. M.; Intia, F.; Park, J. H.; Kropf, A. J.; Kariuki, N.; Huang, Z.; Farghaly, A.; Amichi, L.; Saha, P.; Tao, L.; Cullen, D. A.; Myers, D. J.; Ferrandon, M. S.; Neyerlin, K. C. A Scalable Membrane Electrode Assembly Architecture for Efficient Electrochemical Conversion of CO2 to Formic Acid. *Nat. Commun.* **2023**, *14* (1), No. 7605.

(13) Chen, X.; Cavallo, L.; Huang, K.-W. Selectivity of Electrochemical CO2 Reduction on Metal Electrodes: The Role of the Surface Oxidized Layer. *ACS Catal.* **2023**, *13*, 13089−13100.

(14) Liu, Z.; Zong, X.; Vlachos, D. G.; Filot, I. A. W.; Hensen, E. J. M. A Computational Study of Electrochemical CO2 Reduction to Formic Acid on Metal-Doped SnO2. *Chin. J. Catal.* **2023**, *50*, 249−259.

(15) Liu, H.; Li, B.; Liu, Z.; Liang, Z.; Chuai, H.; Wang, H.; Lou, S. N.; Su, Y.; Zhang, S.; Ma, X. Ceria -Mediated Dynamic Sn0/Snδ+ Redox Cycle for CO2 Electroreduction. *ACS Catal.* **2023**, *13*, 5033−5042.

(16) Zhang, S.; Kang, P.; Meyer, T. J. Nanostructured Tin Catalysts for Selective Electrochemical Reduction of Carbon Dioxide to Formate. *J. Am. Chem. Soc.* **2014**, *136* (5), 1734−1737.

(17) Fang, L.; Lyu, X.; Xu, J. J.; Liu, Y.; Hu, X.; Reinhart, B. J.; Li, T. Operando X-Ray Absorption Spectroscopy Study of SnO2 Nanoparticles for Electrochemical Reduction of CO2 to Formate. *ACS Appl. Mater. Interfaces* **2022**, *14* (50), 55636−55643.

(18) Dutta, A.; Kuzume, A.; Kaliginedi, V.; Rahaman, M.; Sinev, I.; Ahmadi, M.; Roldán Cuenya, B.; Vesztergom, S.; Broekmann, P. Probing the Chemical State of Tin Oxide NP Catalysts during CO2 Electroreduction: A Complementary Operando Approach. *Nano Energy* **2018**, *53*, 828−840.

(19) Jiang, Y.; Shan, J.; Wang, P.; Huang, L.; Zheng, Y.; Qiao, S.-Z. Stabilizing Oxidation State of SnO2 for Highly Selective CO2 Electroreduction to Formate at Large Current Densities. *ACS Catal.* **2023**, *13*, 3101−3108.

(20) Liu, L.-X.; Zhou, Y.; Chang, Y.-C.; Zhang, J.-R.; Jiang, L.-P.; Zhu, W.; Lin, Y. Tuning Sn3O4 for CO2 Reduction to Formate with Ultra-High Current Density. *Nano Energy* **2020**, *77*, No. 105296.

(21) Baruch, M. F.; Pander, J. E.; White, J. L.; Bocarsly, A. B. Mechanistic Insights into the Reduction of CO2 on Tin Electrodes Using in Situ ATR-IR Spectroscopy. *ACS Catal.* **2015**, *5* (5), 3148−3156.

(22) Dutta, A.; Kuzume, A.; Rahaman, M.; Vesztergom, S.; Broekmann, P. Monitoring the Chemical State of Catalysts for CO2 Electroreduction: An In Operando Study. *ACS Catal.* **2015**, *5* (12), 7498−7502.

(23) Chen, Y.; Kanan, M. W. Tin Oxide Dependence of the CO2 Reduction Efficiency on Tin Electrodes and Enhanced Activity for Tin/Tin Oxide Thin-Film Catalysts. *J. Am. Chem. Soc.* **2012**, *134* (4), 1986−1989.

(24) Feaster, J. T.; Shi, C.; Cave, E. R.; Hatsukade, T.; Abram, D. N.; Kuhl, K. P.; Hahn, C.; Nørskov, J. K.; Jaramillo, T. F. Understanding Selectivity for the Electrochemical Reduction of Carbon Dioxide to Formic Acid and Carbon Monoxide on Metal Electrodes. *ACS Catal.* **2017**, *7* (7), 4822−4827.

(25) Salvini, C.; Re Fiorentin, M.; Risplendi, F.; Raffone, F.; Cicero, G. Active Surface Structure of SnO2 Catalysts for CO2 Reduction Revealed by Ab Initio Simulations. *J. Phys. Chem. C* **2022**, *126* (34), 14441−14447.

(26) Nørskov, J. K.; Rossmeisl, J.; Logadottir, A.; Lindqvist, L.; Kitchin, J. R.; Bligaard, T.; Jónsson, H. Origin of the Overpotential for Oxygen Reduction at a Fuel-Cell Cathode. *J. Phys. Chem. B* **2004**, *108* (46), 17886−17892.

(27) Lindgren, P.; Kastlunger, G.; Peterson, A. A. Electrochemistry from the Atomic Scale, in the Electronically Grand-Canonical Ensemble. *J. Chem. Phys.* **2022**, *157* (18), No. 180902.

(28) Tezak, C. R.; Singstock, N. R.; Alherz, A. W.; Vigil-Fowler, D.; Sutton, C. A.; Sundararaman, R.; Musgrave, C. B. Revised Nitrogen Reduction Scaling Relations from Potential-Dependent Modeling of Chemical and Electrochemical Steps. *ACS Catal.* **2023**, *13*, 12894−12903.

(29) Alsunni, Y. A.; Musgrave, C. B. Effect of Applied Potential on Metal Surfaces: Surface Energy, Wulff Shape and Charge Distribution. *Appl. Surf. Sci.* **2023**, *610*, No. 155147.

(30) Alsunni, Y. A.; Alherz, A. W.; Musgrave, C. B. Electrocatalytic Reduction of CO2 to CO over Ag(110) and Cu(211) Modeled by Grand-Canonical Density Functional Theory. *J. Phys. Chem. C* **2021**, *125* (43), 23773−23783.

(31) Brimley, P.; Almajed, H.; Alsunni, Y.; Alherz, A. W.; Bare, Z. J. L.; Smith, W. A.; Musgrave, C. B. Electrochemical CO2 Reduction over Metal-/Nitrogen-Doped Graphene Single-Atom Catalysts Modeled Using the Grand-Canonical Density Functional Theory. *ACS Catal.* **2022**, *12* (16), 10161−10171.

(32) Fishler, Y.; Leick, N.; Teeter, G.; Holewinski, A.; Smith, W. A. Layered Sn-Au Thin Films for Increased Electrochemical ATR-SEIRAS Enhancement. *ACS Appl. Mater. Interfaces* **2024**, *16*, 19780.

(33) Yan, Li. Q.-X.; Huo, S.-J.; Ma, M.; Cai, W.-B.; Osawa, M. Ubiquitous Strategy for Probing ATR Surface-Enhanced Infrared Absorption at Platinum Group Metal−Electrolyte Interfaces. *J. Phys. Chem. B* **2005**, *109* (16), 7900−7906.

(34) Wang, H.; Zhou, Y.-W.; Cai, W.-B. Recent Applications of *in Situ* ATR-IR Spectroscopy in Interfacial Electrochemistry. *Curr. Opin. Electrochem.* **2017**, *1* (1), 73−79.

(35) Miyake, H.; Ye, S.; Osawa, M. Electroless Deposition of Gold Thin Films on Silicon for Surface-Enhanced Infrared Spectroelectrochemistry. *Electrochem. Commun.* **2002**, *4* (12), 973−977.

(36) Dunwell, M.; Yang, X.; Yan, Y.; Xu, B. Potential Routes and Mitigation Strategies for Contamination in Interfacial Specific Infrared Spectroelectrochemical Studies. *J. Phys. Chem. C* **2018**, *122* (43), 24658−24664.

(37) Jerkiewicz, G. Applicability of Platinum as a Counter-Electrode Material in Electrocatalysis Research. *ACS Catal.* **2022**, *12* (4), 2661−2670.

(38) Topalov, A. A.; Katsounaros, I.; Auinger, M.; Cherevko, S.; Meier, J. C.; Klemm, S. O.; Mayrhofer, K. J. J. Dissolution of Platinum: Limits for the Deployment of Electrochemical Energy Conversion? *Angew. Chem., Int. Ed.* **2012**, *51* (50), 12613−12615.

(39) Duan, Z.; Henkelman, G. Atomic-Scale Mechanisms of Electrochemical Pt Dissolution. *ACS Catal.* **2021**, *11* (23), 14439−14447.

(40) Sundararaman, R.; Letchworth-Weaver, K.; Schwarz, K. A.; Gunceler, D.; Ozhabes, Y.; Arias, T. A. JDFTx: Software for Joint Density-Functional Theory. *SoftwareX* **2017**, *6*, 278−284.

(41) Perdew, J. P.; Burke, K.; Ernzerhof, M. Generalized Gradient Approximation Made Simple. *Phys. Rev. Lett.* **1996**, *77* (18), 3865−3868.

(42) Grimme, S.; Antony, J.; Ehrlich, S.; Krieg, H. A Consistent and Accurate Ab Initio Parametrization of Density Functional Dispersion Correction (DFT-D) for the 94 Elements H-Pu. *J. Chem. Phys.* **2010**, *132* (15), No. 154104.

(43) Garrity, K. F.; Bennett, J. W.; Rabe, K. M.; Vanderbilt, D. Pseudopotentials for High-Throughput DFT Calculations. *Comput. Mater. Sci.* **2014**, *81*, 446−452.

(44) Sundararaman, R.; Goddard, W. A. The Charge-Asymmetric Nonlocally Determined Local-Electric (CANDLE) Solvation Model. *J. Chem. Phys.* **2015**, *142* (6), No. 064107.

(45) Jain, A.; Ong, S. P.; Hautier, G.; Chen, W.; Richards, W. D.; Dacek, S.; Cholia, S.; Gunter, D.; Skinner, D.; Ceder, G.; Persson, K.

A. Commentary: The Materials Project: A Materials Genome Approach to Accelerating Materials Innovation. *APL Mater.* **2013**, *1* (1), No. 011002.

(46) Rhodes, K. J.; Meisner, R.; Kirkham, M.; Dudney, N.; Daniel, C. In Situ XRD of Thin Film Tin Electrodes for Lithium Ion Batteries. *J. Electrochem. Soc.* **2012**, *159* (3), A294.

(47) Shieh, S. R.; Kubo, A.; Duffy, T. S.; Prakapenka, V. B.; Shen, G. High-pressure phases in to 117 GPa. *Phys. Rev. B* **2006**, *73* (1), No. 014105, DOI: 10.1103/PhysRevB.73.014105.

(48) Haines, J.; Léger, J. M. X-Ray Diffraction Study of the Phase Transitions and Structural Evolution of Tin Dioxide at High Pressure:ffRelationships between Structure Types and Implications for Other Rutile-Type Dioxides. *Phys. Rev. B* **1997**, *55* (17), 11144−11154.

(49) Eckold, P.; Sellers, M. S.; Niewa, R.; Hügel, W. The surface energies of β-Sn—A new concept for corrosion and whisker mitigation. *Microelectron. Reliab.* **2015**, *55* (12), 2799−2807, DOI: 10.1016/j.microrel.2015.08.018.

(50) Oviedo, J.; Gillan, M. J. Energetics and Structure of Stoichiometric SnO_2 Surfaces Studied by First-Principles Calculations. *Surf. Sci.* **2000**, *463* (2), 93−101.

(51) Tran, R.; Xu, Z.; Radhakrishnan, B.; Winston, D.; Sun, W.; Persson, K. A.; Ong, S. P. Surface Energies of Elemental Crystals. *Sci. Data* **2016**, *3* (1), No. 160080.

(52) Larsen, A. H.; Mortensen, J. J.; Blomqvist, J.; Castelli, I. E.; Christensen, R.; Dułak, M.; Friis, J.; Groves, M. N.; Hammer, B.; Hargus, C.; Hermes, E. D.; Jennings, P. C.; Jensen, P. B.; Kermode, J.; Kitchin, J. R.; Kolsbjerg, E. L.; Kubal, J.; Kaasbjerg, K.; Lysgaard, S.; Maronsson, J. B.; Maxson, T.; Olsen, T.; Pastewka, L.; Peterson, A.; Rostgaard, C.; Schiøtz, J.; Schütt, O.; Strange, M.; Thygesen, K. S.; Vegge, T.; Vilhelmsen, L.; Walter, M.; Zeng, Z.; Jacobsen, K. W. The atomic simulation environment—a Python library for working with atoms. *J. Phys.: Condens.Matter* **2017**, *29* (27), No. 273002, DOI: 10.1088/1361-648X/aa680e.

(53) Lindan, P. J. D. Water Chemistry at the $SnO_2(110)$ Surface: The Role of Inter-Molecular Interactions and Surface Geometry. *Chem. Phys. Lett.* **2000**, *328* (4), 325−329.

(54) Lindan, P. J. D.; Harrison, N. M.; Gillan, M. J. Mixed Dissociative and Molecular Adsorption of Water on the Rutile (110) Surface. *Phys. Rev. Lett.* **1998**, *80* (4), 762−765.

(55) Zhang, C.; Lindan, P. J. D. Towards a First-Principles Picture of the Oxide−Water Interface. *J. Chem. Phys.* **2003**, *119* (17), 9183−9190.

(56) Whittaker, T.; Kumar, K. B. S.; Peterson, C.; Pollock, M. N.; Grabow, L. C.; Chandler, B. D. H_2 Oxidation over Supported Au Nanoparticle Catalysts: Evidence for Heterolytic H_2 Activation at the Metal−Support Interface. *J. Am. Chem. Soc.* **2018**, *140* (48), 16469−16487.

(57) Chen, J.; Cheng, C.; Bai, Y.-M.; Liu, H.; Dong, C.; Du, X.-W. Identifying a Key Factor Determining Interfacial Electron Transfer in CO_2 Reduction to Formate: Potential of Zero Charge. *J. Phys. Chem. C* **2023**, *127*, 9623.

(58) Evans, M. G.; Polanyi, M. Inertia and Driving Force of Chemical Reactions. *Trans. Faraday Soc.* **1938**, *34*, 11−24, DOI: 10.1039/tf9383400011.

(59) Bligaard, T.; Nørskov, J. K.; Dahl, S.; Matthiesen, J.; Christensen, C. H.; Sehested, J. The Brønsted−Evans−Polanyi Relation and the Volcano Curve in Heterogeneous Catalysis. *J. Catal.* **2004**, *224* (1), 206−217.

(60) Liu, Z.-P.; Hu, P. General Trends in the Barriers of Catalytic Reactions on Transition Metal Surfaces. *J. Chem. Phys.* **2001**, *115* (11), 4977−4980.

(61) Quan, J.; Muttaqien, F.; Kondo, T.; Kozarashi, T.; Mogi, T.; Imabayashi, T.; Hamamoto, Y.; Inagaki, K.; Hamada, I.; Morikawa, Y.; Nakamura, J. Vibration-Driven Reaction of CO_2 on Cu Surfaces via Eley−Rideal-Type Mechanism. *Nat. Chem.* **2019**, *11* (8), 722−729.

(62) Domínguez-Flores, F.; Melander, M. M. Approximating Constant Potential DFT with Canonical DFT and Electrostatic Corrections. *J. Chem. Phys.* **2023**, *158* (14), No. 144701.

(63) Durst, J.; Siebel, A.; Simon, C.; Hasché, F.; Herranz, J.; Gasteiger, H. A. New Insights into the Electrochemical Hydrogen Oxidation and Evolution Reaction Mechanism. *Energy Environ. Sci.* **2014**, *7* (7), 2255−2260.

(64) Azizi, O.; Jafarian, M.; Gobal, F.; Heli, H.; Mahjani, M. G. The Investigation of the Kinetics and Mechanism of Hydrogen Evolution Reaction on Tin. *Int. J. Hydrogen Energy* **2007**, *32* (12), 1755−1761.

(65) Wuttig, A.; Yoon, Y.; Ryu, J.; Surendranath, Y. Bicarbonate Is Not a General Acid in Au-Catalyzed CO_2 Electroreduction. *J. Am. Chem. Soc.* **2017**, *139* (47), 17109−17113.

(66) Shan, W.; Liu, R.; Zhao, H.; Liu, J. Bicarbonate Rebalances the *COOH/*OCO− Dual Pathways in CO_2 Electrocatalytic Reduction: In Situ Surface-Enhanced Raman Spectroscopic Evidence. *J. Phys. Chem. Lett.* **2022**, *13* (31), 7296−7305.

(67) Monteiro, M. C.; Mirabal, A.; Jacobse, L.; Doblhoff-Dier, K.; Barton, S. C.; Koper, M. T. Time-Resolved Local pH Measurements during CO_2 Reduction Using Scanning Electrochemical Microscopy: Buffering and Tip Effects. *JACS Au* **2021**, *1*, 1915−1924, DOI: 10.1021/jacsau.1c00289.

(68) Yang, K.; Kas, R.; Smith, W. A. In Situ Infrared Spectroscopy Reveals Persistent Alkalinity near Electrode Surfaces during CO_2 Electroreduction. *J. Am. Chem. Soc.* **2019**, *141* (40), 15891−15900.

(69) Webb, J. D.; Gedvilas, L. M.; Crandall, R. S.; Iwaniczko, E.; Nelson, B. P.; Mahan, A. H.; Reedy, R.; Matson, R. J. Anisotropy in Hydrogenated Amorphous Silicon Films as Observed Using Polarized Ftir-Atr Spectroscopy. *MRS Online Proc. Libr.* **1999**, *557*, 311 DOI: 10.1557/PROC-557-311.

(70) Pennathur, A. K.; Tseng, C.; Salazar, N.; Dawlaty, J. M. Controlling Water Delivery to an Electrochemical Interface with Surfactants. *J. Am. Chem. Soc.* **2023**, *145* (4), 2421−2429.

(71) Ge, W.; Chen, Y.; Fan, Y.; Zhu, Y.; Liu, H.; Song, L.; Liu, Z.; Lian, C.; Jiang, H.; Li, C. Dynamically Formed Surfactant Assembly at the Electrified Electrode−Electrolyte Interface Boosting CO_2 Electroreduction. *J. Am. Chem. Soc.* **2022**, *144* (14), 6613−6622.

(72) Jiang, T.-W.; Qin, X.; Ye, K.; Zhang, W.-Y.; Li, H.; Liu, W.; Huo, S.; Zhang, X.-G.; Jiang, K.; Cai, W.-B. An Interactive Study of Catalyst and Mechanism for Electrochemical CO_2 Reduction to Formate on Pd Surfaces. *Appl. Catal., B* **2023**, *334*, No. 122815, DOI: 10.1016/j.apcatb.2023.122815.

(73) Cao, C.; Ma, D.-D.; Gu, J.-F.; Xie, X.; Zeng, G.; Li, X.; Han, S.-G.; Zhu, Q.-L.; Wu, X.-T.; Xu, Q. Metal−Organic Layers Leading to Atomically Thin Bismuthene for Efficient Carbon Dioxide Electroreduction to Liquid Fuel. *Angew. Chem., Int. Ed.* **2020**, *59* (35), 15014−15020.

(74) Vijay, S.; Kastlunger, G.; Chan, K.; Nørskov, J. K. Limits to Scaling Relations between Adsorption Energies? *J. Chem. Phys.* **2022**, *156* (23), No. 231102.

(75) Liu, F.; Ren, X.; Zhao, J.; Wu, H.; Wang, J.; Han, X.; Deng, Y.; Hu, W. Inhibiting Sulfur Dissolution and Enhancing Activity of SnS for CO_2 Electroreduction via Electronic State Modulation. *ACS Catal.* **2022**, *12* (21), 13533−13541.

(76) Li, K.; Xu, J.; Zheng, T.; Yuan, Y.; Liu, S.; Shen, C.; Jiang, T.; Sun, J.; Liu, Z.; Xu, Y.; Chuai, M.; Xia, C.; Chen, W. In Situ Dynamic Construction of a Copper Tin Sulfide Catalyst for High-Performance Electrochemical CO_2 Conversion to Formate. *ACS Catal.* **2022**, *12* (16), 9922−9932.

(77) Atrak, N.; Tayyebi, E.; Skúlason, E. Insight into Catalytic Active Sites on TiO_2/RuO_2 and SnO_2/RuO_2 Alloys for Electrochemical CO_2 Reduction to CO and Formic Acid. *ACS Catal.* **2023**, *13*, 5491−5501.

(78) Kim, C.; Bui, J. C.; Luo, X.; Cooper, J. K.; Kusoglu, A.; Weber, A. Z.; Bell, A. T. Tailored Catalyst Microenvironments for CO_2 Electroreduction to Multicarbon Products on Copper Using Bilayer Ionomer Coatings. *Nat. Energy* **2021**, *6* (11), 1026−1034.